

# PHYSICS-INFORMED DEEP DIFFUSION MRI RECONSTRUCTION: BREAK THE BOTTLENECK OF TRAINING DATA IN ARTIFICIAL INTELLIGENCE

Chen Qian<sup>1</sup>, Zi Wang<sup>1</sup>, Xinlin Zhang<sup>1</sup>, Qingrui Cai<sup>1</sup>, Taishan Kang<sup>2</sup>, Boyu Jiang<sup>3</sup>, Ran Tao<sup>3</sup>, Zhigang Wu<sup>4</sup>, Di Guo<sup>5</sup>, and Xiaobo Qu<sup>1\*</sup>  
 Department of Electronic Science, Fujian Key Laboratory of Plasma and Magnetic Resonance, Xiamen University<sup>1</sup>. Department of Radiology, Zhongshan Hospital affiliated to Xiamen University<sup>2</sup>. United Imaging Healthcare<sup>3</sup>. Philips, Beijing, China<sup>4</sup>. School of Computer and Information Engineering, Xiamen University of Technology<sup>5</sup>.

## ABSTRACT

In this work, we propose a Physics-Informed Deep Diffusion magnetic resonance imaging (DWI) reconstruction method (PIDD). PIDD contains two main components: The multi-shot DWI data synthesis and a deep learning reconstruction network. For data synthesis, we first mathematically analyze the motion during the multi-shot data acquisition and approach it by a simplified physical motion model. The motion model inspires a polynomial model for motion-induced phase synthesis. Then, lots of synthetic phases are combined with a few real data to generate a large amount of training data. For reconstruction network, we exploit the smoothness property of each shot image phase as learnable convolution kernels in the k-space and complementary sparsity in the image domain. Results on both synthetic and *in vivo* brain data show that, the proposed PIDD trained on synthetic data enables sub-second ultra-fast, high-quality, and robust reconstruction with different b-values and undersampling patterns.

**Index Terms**—Physical-informed, synthetic data, deep learning, diffusion MRI reconstruction

## 1. INTRODUCTION

The past several years have witnessed the great achievements made by deep learning in biomedical magnetic resonance image (MRI) [1-4] and spectrum [5-8] reconstructions. However, unavailable or insufficient high-quality training data is still one of its bottlenecks in some scenarios [9], including our concerned high-resolution diffusion MRI (DWI) with multi-shot interleaved echo planer imaging (Ms-iEPI) techniques. DWI has been widely employed in clinical diagnosis of cancer [10, 11] and the scientific research of brain fiber tractography [12]. In Ms-iEPI DWI, accurate training data are unavailable due to inter-shot motion artifacts [13, 14] caused by phase variations between shots.

To overcome the data bottleneck in Ms-iEPI DWI, reconstruction results of traditional optimization-based methods are employed as labels for network training [15, 16]. However, the quality of training dataset is limited by the traditional methods. Moreover, in high b-values (3000 s/mm<sup>2</sup>) and undersampling DWI, it is hard for traditional methods to provide high-quality reconstruction results [17, 18].

Recently, imaging physics-based data synthesis (IPADS) [9] emerges as a novel paradigm. Following the physical

mechanism, it provides numerous high-quality training data without or with a few real data, and has shown great potential in biomedical MRI [9].

In this work, inspired by IPADS, we propose a physics-informed deep diffusion MRI reconstruction method (PIDD) to overcome the data bottleneck in the deep learning reconstruction of Ms-iEPI DWI. For data synthesis, the motion during the Ms-iEPI data acquisition is analyzed and approached by a simplified physical model. Then, the motion-induced phase variations (motion phase) are synthesized by a physics-informed polynomial phase model (Fig. 1). Finally, lots of synthetic motion phase is generated and combined with a few real data to provide a large amount of training data. After generating training data, we design a reconstruction network which exploits the smoothness property of each shot image phase (shot phase) as learnable convolution kernels in the k-space and complementary sparsity in the image domain.

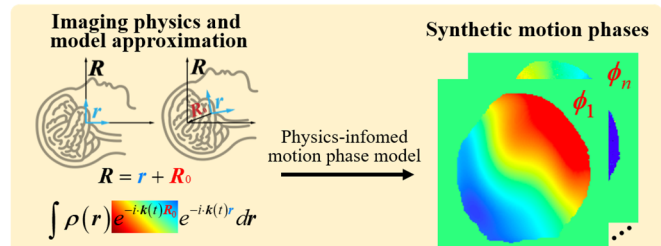


Fig. 1. The schematic of physics-informed motion phase synthesis in PIDD.  $r$  and  $R$  represent the subject and the scanner coordinate systems, respectively.  $R_0$  is the motion-induced position change of  $r$  and  $R$ .  $\rho(r)$  is the relaxation and diffusion-weighted transverse magnetization at  $r$ , and  $k(t)$  is the k-space position.

Results on the synthetic data show that the proposed PIDD owns the highest PSNR among compared state-of-the-art methods. Besides, PIDD trained on synthetic data generalizes well to *in vivo* brain data with different b-values (1000-3000 s/mm<sup>2</sup>) and undersampling patterns (partial Fourier with 0.6 and 0.75 sampling rates).

## 2. PHYSICS-INFORMED DATA SYNTHESIS

In this section, we first mathematically analyze the origin and properties of the motion phase between shots. Then, the physics-informed polynomial phase model is designed considering the physical mechanism of the motion during shots acquisition. At last, the whole Ms-iEPI DWI data

synthesis process is presented.

### 2.1. Physical mechanism of inter-shots motion

Suppose the coordinates in the subject and the scanner coordinate systems are  $\mathbf{r}$  and  $\mathbf{R}$ , respectively. Motions during scanning introduce the relative positional relationship in two coordinate systems:  $\mathbf{R} = \mathbf{r} + \mathbf{R}_0(\mathbf{r}, t)$ .

Thus, the acquired k-space signal is [13]:

$$\mathbf{y}(t) = \int \rho(\mathbf{r}) e^{-i\mathbf{k}(t)\mathbf{R}_0(\mathbf{r}, t)} e^{-i\mathbf{k}(t)\mathbf{r}} d\mathbf{r}, \quad (1)$$

where  $\rho(\mathbf{r})$  is the relaxation and diffusion-weighted transverse magnetization at  $\mathbf{r}$ , and  $\mathbf{k}(t)$  is the k-space position at time  $t$ .

The accumulated motion-induced extra phase of the  $j$ -th shot denotes [13]:

$$\begin{aligned} \phi_j(\mathbf{r}) &= \exp(i \cdot (\mathbf{R}_0(\mathbf{r}, t)\mathbf{k}(t))) \\ &= \exp(i \cdot (\gamma \int \mathbf{R}_0(\mathbf{r}, t)\mathbf{g}(t) dt)), \end{aligned} \quad (2)$$

where  $\gamma$  is the gyromagnetic ratio and  $\mathbf{g}$  is the diffusion gradients. The order of  $\phi_j(\mathbf{r})$  is only determined by  $\mathbf{r}$  in  $\mathbf{R}_0(\mathbf{r}, t)$ , namely the relative motion between the subject and scanner.

In brain imaging, the motion could be simplified as shifts (zero-order of  $\mathbf{r}$ ) and rotations (one-order of  $\mathbf{r}$ ), due to the brain can be approximated as a rigid body [13]. Thus, the motion phase  $\phi_j(\mathbf{r})$  could be represented as a polynomial with respect to  $\mathbf{r}$ .

### 2.2. Polynomial motion phase model

We propose a polynomial motion phase model here, and the  $j$ -th shot motion phase  $\phi_j(\mathbf{r})$  is:

$$\phi_j(x, y) = \exp\left\{i \cdot \left(\sum_{l=0}^L \sum_{m=0}^l (A_{lm} x^m y^{l-m})\right)\right\}, \quad (3)$$

where  $\mathbf{r}$  is replaced by coordinates  $(x, y)$ ,  $L$  is the order of the polynomial, and  $A_{lm}$  is the coefficient of the  $x^m y^{l-m}$ .

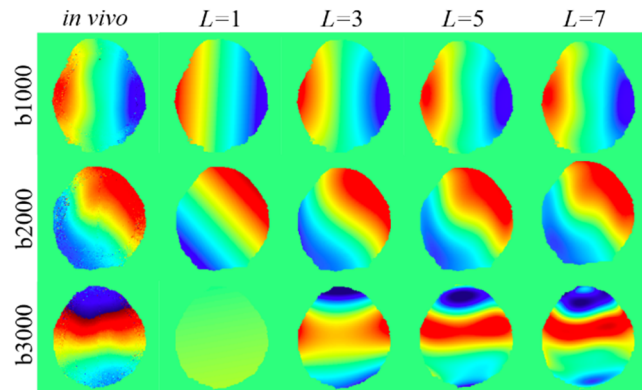


Fig. 2. Representative motion phases of 4-shot DWI with different b-values (1000, 2000, 3000 s/mm<sup>2</sup>) and corresponding synthetic motion phases with different polynomial order ( $L = 1, 3, 5, 7$ ).

The motion phase model is employed to fit the *in vivo* motion phases of the multi-shot DWI images with different

b-values (Fig. 2). The larger  $L$  shows a better fitting ability for the complex shot phase.  $L=7$  is selected for the balance of computational complexity and accuracy in the following motion phase generation.

### 2.3. Physics-informed data synthesis

The  $j$ -th shot image  $\mathbf{I}_j$  can be represented as:

$$\mathbf{I}_j = e^{-i\phi_j} e^{-i\varphi} \mathbf{m} = \mathbf{P}_j \mathbf{m}, \quad (4)$$

where  $\mathbf{m}$  is the magnitude image shared by all shot images, background phase  $e^{-i\varphi}$  and motion phase  $e^{-i\phi_j}$  combined to be the shot phase  $\mathbf{P}_j$ . Since both the background phase and motion phase are commonly assumed to be smooth and vary slowly [17],  $\mathbf{P}_j$  is approximately smooth too.

The whole multi-shot DWI data synthesis process is as follows: (1) Reconstruct complex  $\mathbf{B}_0$  images (b-value = 0 s/mm<sup>2</sup>) with background phase. (2) Multiply these complex images with coil sensitivity maps that are estimated from real multi-channel k-space by ESPRIT [19], such as the  $\mathbf{B}_0$  data. (3) Multiply each channel image with the synthetic motion phases to get each shot data. (4) Transform each shot image of each channel into k-space and then add Gaussian noise.

## 3. RECONSTRUCTION NETWORK

In this section, the shot phase in the image domain is modelled as the motion kernel in the k-space. Furthermore, a reconstruction network based on motion kernel learning in the k-space and sparsity in the image domain is proposed.

### 3.1. Motion kernels from shot phases

The  $i$ -th and  $j$ -th shot images have a relationship:

$$\mathbf{I}_i = \mathbf{P}_i \mathbf{m} = \mathbf{P}_i \frac{\mathbf{P}_j^\dagger}{\mathbf{P}_j^\dagger \mathbf{P}_j} \mathbf{P}_j \mathbf{m} = \mathbf{P}_i \frac{\mathbf{P}_j^\dagger}{\mathbf{P}_j^\dagger \mathbf{P}_j} \mathbf{I}_j = \hat{\mathbf{P}}_{ij} \mathbf{I}_j. \quad (5)$$

where the superscript  $\dagger$  is the complex conjugate.

Transform Eq. (5) into the k-space, and we get the relationship of two shot images in convolution version:

$$\mathbf{X}_i = \mathcal{G}_{ij} \mathbf{X}_j, \quad (6)$$

where  $\mathbf{X}_i$  and  $\mathbf{X}_j$  are the Fourier transform of the  $\mathbf{I}_i$  and  $\mathbf{I}_j$  in the k-space, and  $\mathcal{G}_{ij}$  is the convolution operator of  $\hat{\mathbf{P}}_{ij}$ .

The non-zero values of  $\mathcal{G}_{ij}$  in the k-space are concentrated in the limited support due to the smoothness of the  $\hat{\mathbf{P}}_{ij}$  [14, 17, 20]. Thus,  $\mathcal{G}_{ij}$  could be approached by  $\hat{\mathcal{G}}_{ij}$  with limited support. Then, Eq. (6) becomes:

$$\mathbf{X}_i \approx \hat{\mathcal{G}}_{ij} \mathbf{X}_j. \quad (7)$$

Furthermore, we build a structured matrix  $\mathcal{P}$  consisting of shot phase modulation  $\hat{\mathbf{P}}_{ij}$  to represent the relationships between all shot images:

$$\mathcal{P}\mathbf{I} = \frac{1}{J-1} \begin{bmatrix} 0 & \hat{\mathbf{P}}_{12} & \hat{\mathbf{P}}_{13} & \cdots & \hat{\mathbf{P}}_{1J} \\ \hat{\mathbf{P}}_{21} & 0 & \hat{\mathbf{P}}_{23} & \cdots & \hat{\mathbf{P}}_{2J} \\ \hat{\mathbf{P}}_{31} & \hat{\mathbf{P}}_{32} & 0 & \cdots & \hat{\mathbf{P}}_{3J} \\ \vdots & \vdots & \vdots & 0 & \vdots \\ \hat{\mathbf{P}}_{J1} & \hat{\mathbf{P}}_{J2} & \hat{\mathbf{P}}_{J3} & \cdots & 0 \end{bmatrix} \begin{bmatrix} \mathbf{I}_1 \\ \vdots \\ \mathbf{I}_j \\ \vdots \\ \mathbf{I}_J \end{bmatrix} = \begin{bmatrix} \mathbf{I}_1 \\ \vdots \\ \mathbf{I}_j \\ \vdots \\ \mathbf{I}_J \end{bmatrix}. \quad (8)$$

Perform the Fourier transform on Eq. (8) by substituting multiplication in the image space with the convolution operator in Eq. (6), we get the relationships of all shots in the k-space:

$$\mathcal{G}\mathbf{X} = \frac{1}{J-1} \begin{bmatrix} 0 & \mathcal{G}_{12} & \mathcal{G}_{13} & \cdots & \mathcal{G}_{1J} \\ \mathcal{G}_{21} & 0 & \mathcal{G}_{23} & \cdots & \mathcal{G}_{2J} \\ \mathcal{G}_{31} & \mathcal{G}_{32} & 0 & \cdots & \mathcal{G}_{3J} \\ \vdots & \vdots & \vdots & 0 & \vdots \\ \mathcal{G}_{J1} & \mathcal{G}_{J2} & \mathcal{G}_{J3} & \cdots & 0 \end{bmatrix} \begin{bmatrix} \mathbf{X}_1 \\ \vdots \\ \mathbf{X}_j \\ \vdots \\ \mathbf{X}_J \end{bmatrix} = \begin{bmatrix} \mathbf{X}_1 \\ \vdots \\ \mathbf{X}_j \\ \vdots \\ \mathbf{X}_J \end{bmatrix}. \quad (9)$$

Finally, we get the motion kernel  $\hat{\mathcal{G}}$  by approaching approximately of  $\mathcal{G}$  with limited support:

$$\hat{\mathcal{G}}\mathbf{X} \approx \mathbf{X}. \quad (10)$$

The  $\hat{\mathcal{G}}$  derived from the motion phase provides the interpolation kernels between the shot images in the k-space.

### 3.2. Ms-iEPI DWI reconstruction network

The motion kernel calculated from the shot phase of the reconstructed images in Eq. (10) are unavailable before reconstruction. Thus, we employ a motion kernel learning module consisting of groups of learnable convolution kernels for DWI image reconstruction (Fig. 3(b)).

To improve the reconstruction performance further, a deep sparse module (Fig. 3(c)) [3] and a data consistency module (Fig. 3(d)) are employed.

Finally, we obtain a reconstruction network with  $K$  blocks (Fig. 3), and each block has three modules. The details about each module are as follows:

#### 1) Motion kernel estimation module

The motion kernels are learned by network  $\mathcal{N}_1$ :

$$\mathbf{Z}_1^k = \mathcal{N}_1(\mathbf{X}^{k-1}), \quad (11)$$

where  $k$  donates the number of the block. The input  $\mathbf{X}^{k-1}$  is the output of the  $k-1$  block.

The  $\mathcal{N}_1$  has 6 layers, and each layer is composed of 3 groups of 24 convolution kernels of size 1, 3, and 5, respectively (Fig. 3(b)). The parameters can be updated in the supervised training stage by learning the motion kernels. In the reconstruction stage, these convolution kernels in  $\mathcal{N}_1$  play the role of motion kernel  $\hat{\mathcal{G}}$  to do interpolation among the shot images in the k-space. The output  $\mathbf{Z}_1^k$  is the multi-shot k-space after the interpolation.

#### 2) Deep sparse module

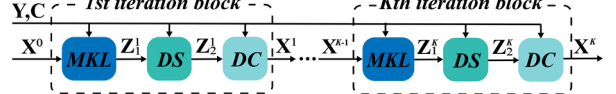
We employ an encoder and decoder architecture to

constrain the sparsity of images in the image domain:

$$\mathbf{Z}_2^k = \mathcal{F}\mathcal{N}_3[\text{soft}(\mathcal{N}_2(\mathcal{F}^{-1}\mathbf{Z}_1^k); r^k)], \quad (12)$$

where  $\text{soft}(\cdot; r^k)$  is the soft-thresholding operator [3], and  $r^k$  is the learnable threshold initialized to 0.001.  $\mathcal{F}$  is the Fourier transform operator,  $\mathcal{F}^{-1}$  is the inverse Fourier transform operator.  $\mathcal{N}_3$  has a symmetrical structure as  $\mathcal{N}_2$  (Fig. 3(c)). Both  $\mathcal{N}_2$  and  $\mathcal{N}_3$  have three layers and each layer contains 24 convolution kernels of size 3.

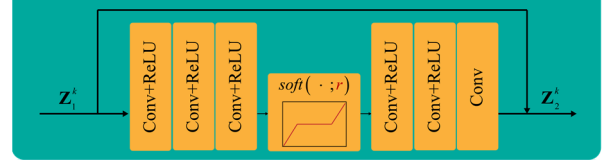
#### (a) Network architecture:



#### (b) Motion kernel learning module: $\mathbf{Z}_1^k = \mathcal{N}_1(\mathbf{X}^{k-1})$



#### (c) Deep sparse module: $\mathbf{Z}_2^k = \mathcal{F}\mathcal{N}_3[\text{soft}(\mathcal{N}_2(\mathcal{F}^{-1}\mathbf{Z}_1^k); r^k)]$



#### (d) Data consistency module:

$$\mathbf{X}^k = (\mathcal{F}\mathbf{C}^* \mathcal{F}^{-1} \mathbf{U}^* \mathcal{U} \mathcal{F} \mathbf{C} \mathcal{F}^{-1} + \lambda_1 \mathbf{D})^{-1} (\mathcal{F}\mathbf{C}^* \mathcal{F}^{-1} \mathbf{U}^* \mathbf{Y} + \lambda_1 \mathbf{Z}_2^k)$$

Fig. 3. The architecture of the reconstruction network. (a) The recursive block includes (b) motion kernel learning module, (c) deep sparse (DS) module, and (d) data consistency (DC) module. Note: The variables marked red are learnable. Conv is the convolution.

#### 3) Data consistency module

A conjugate gradient algorithm is used as a data consistency module [21] (Fig. 3(d)):

$$\mathbf{X}^k = (\mathcal{F}\mathbf{C}^* \mathcal{F}^{-1} \mathbf{U}^* \mathcal{U} \mathcal{F} \mathbf{C} \mathcal{F}^{-1} + \lambda_1 \mathbf{D})^{-1} (\mathcal{F}\mathbf{C}^* \mathcal{F}^{-1} \mathbf{U}^* \mathbf{Y} + \lambda_1 \mathbf{Z}_2^k), \quad (13)$$

where  $\mathbf{D}$  is the identity matrix,  $\mathbf{Y}$  is the multi-channel multi-shot sampled k-space data,  $\mathbf{C}$  is the sensitivity maps,  $\mathcal{U}$  is the undersampling operator, the superscript  $*$  is the adjoint operation, the regularization parameter  $\lambda_1$  is set to 0.01.

The loss employed for reconstruction network training contains two parts:

$$\mathcal{L} = \frac{1}{KT} \sum_{t=1}^T \sum_{k=1}^K \left( \|\mathbf{X}^{k,t} - \mathbf{X}_{GT}^t\|_F^2 + \beta \|\mathcal{N}_1(\mathbf{X}_{GT}^{t,k}) - \mathbf{X}_{GT}^t\|_F^2 \right), \quad (14)$$

where  $T$  is the number of training samples. The  $\mathbf{X}^{k,t}$  is the output of the  $k$ -th block with  $t$ -th training samples as input. The  $\mathcal{N}_1(\mathbf{X}_{GT}^{t,k})$  is the output of  $\mathcal{N}_1$  in the  $k$ -th block with the  $t$ -th label  $\mathbf{X}_{GT}^t$  as input.  $\beta$  is set as 0.01.

In the training stage, the weights of reconstruction network

are Xavier initialized and trained for 100 epochs by the Adam optimizer with an initial learning rate of 0.001 and exponential decay of 0.99. The batch size is 1, block number  $K$  is 5, and the whole training process takes about 8 hours on an Nvidia Tesla T4 GPU (16 GB memory) in TensorFlow 1.15.0.

## 4. RESULTS

### 4.1. Generation of synthetic datasets

The reconstruction network trained on the 4-shot synthetic datasets is abbreviated as PIDD, and the synthetic datasets is generated according to Section 2.3.

The 144  $B_0$  images are acquired from 6 subjects by the 4-shot DWI sequence at a 3.0 T MRI (Philips, Ingenia CX) with 32 coils. The TR/TE is 3000/77 ms, and the resolution is  $1.2 \times 1.2 \times 5$  mm<sup>3</sup>. The original size of each slice is  $180 \times 180 \times 32$  and is reduced to  $160 \times 160 \times 4$  by center-cropping and coil compressing to reduce computational complexity. All the *in vivo* data acquisition in this study are Institutional Review Board approved.

For each  $B_0$  image, ten motion phases are generated according to Eq. (3): For  $l = 1, 2, 3, 4, 5, 6, 7$ ,  $A_{lm}$  are randomly distributed in  $[-\pi, \pi)$ ,  $[-\pi, \pi)$ ,  $[-\pi/2, \pi/2)$ ,  $[-\pi/2, \pi/2)$ ,  $[-\pi/2, \pi/2)$ ,  $[-\pi/3, \pi/3)$ ,  $[-\pi/3, \pi/3)$ ,  $[-\pi/3, \pi/3)$ . The Gaussian noise with mean 0 and variance 0.01 is added in the k-space to modeling the noise in the high b-value data.

The synthetic dataset contains 1440 images: 1200 synthesized from five subjects are for training and validation, and 240 from the last subject are for testing.

### 4.2. Comparison study on synthetic data

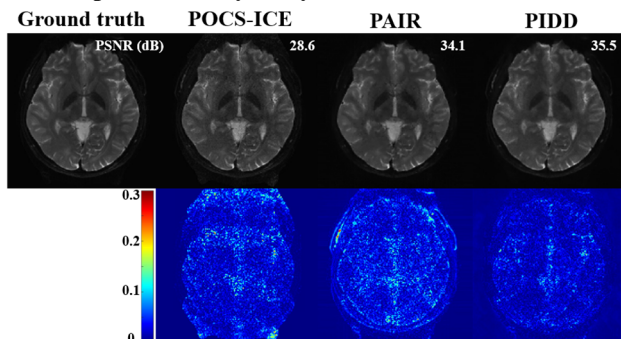


Fig. 4. Comparison study on the synthetic 4-shot testing dataset. PSNRs (dB) in images are the average of random 12 slices.

Fig. 4 shows that, compared with state-of-the-art optimization-based methods POCS-ICE [22] and PAIR [17], the proposed PIDD has better PSNR [23], indicating its good noise suppression ability. Moreover, our PIDD (0.1 second/slice) has much faster reconstruction speed than POCS-ICE (19.0 seconds/slice), and PAIR (40.2 seconds/slice).

### 4.3. Generalization study on multi b-value *in vivo* data

The proposed PIDD is also tested on a 3.0T *in vivo* 4-shot DWI dataset (United Imaging, uMR 790): resolution is  $1.4 \times 1.4 \times 5$  mm, matrix size is  $160 \times 160$ , the channel number is

17, diffusion direction is 3, and b-values are 1000, 2000, and 3000 s/mm<sup>2</sup>. Retrospective partial Fourier sampling with sampling rates of 0.75 and 0.6 are employed in the training and testing of PIDD, respectively.

Fig. 5 shows that, PIDD trained on synthetic data generalizes well on the reconstruction of *in vivo* brain data with different b-values and undersampling patterns.

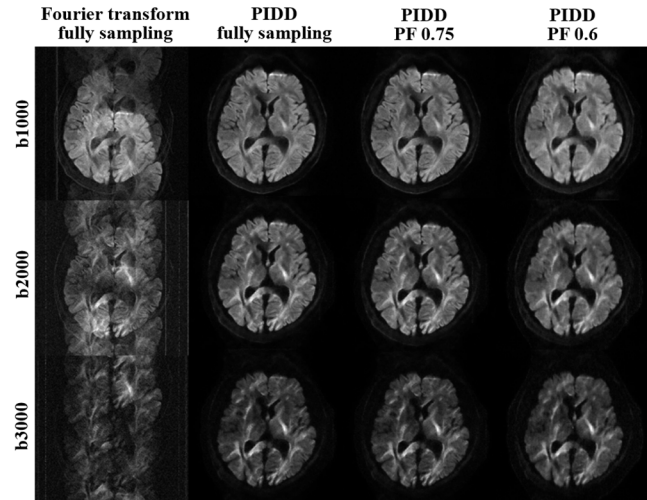


Fig. 5. Reconstructions of 4-shot DWI with b-values 1000, 2000, and 3000 s/mm<sup>2</sup> by PIDD. Note: PF is the partial Fourier undersampling.

## 5. CONCLUSION

We demonstrate that the deep network training for DWI reconstruction can be achieved using synthetic data. The proposed Physics-Informed Deep Diffusion MRI reconstruction method (PIDD) overcomes the data bottleneck of deep learning methods, and enables sub-second ultra-fast reconstruction. PIDD shows promising generalization on *in vivo* brain data with different b-values and undersampling patterns.

## ACKNOWLEDGEMENTS

This work is supported in part by the National Natural Science Foundation of China under grants 62122064, 61971361, and 61871341, Natural Science Foundation of Fujian Province of China under grants 2021J011184, President Fund of Xiamen University under grant 0621ZK1035, and Xiamen University Nanqiang Outstanding Talents Program. The corresponding author is Xiaobo Qu (Email: quxiaobo@xmu.edu.cn).

## REFERENCES

- [1] S. Wang *et al.*, “Accelerating magnetic resonance imaging via deep learning,” in *13th IEEE International Symposium on Biomedical Imaging (ISBI)*, 2016, pp. 514-517.
- [2] B. Zhu, J. Z. Liu, S. F. Cauley, B. R. Rosen, and M. S. Rosen, “Image reconstruction by domain-transform manifold learning,” *Nature*, vol. 555, no. 7697, pp. 487-492, 2018.
- [3] Z. Wang *et al.*, “One-dimensional deep low-rank and sparse network for accelerated MRI,” *IEEE Trans. Med. Imaging*, DOI:10.1109/TMI.2022.3203312, 2022.

- [4] T. Lu *et al.*, “pFISTA-SENSE-ResNet for parallel MRI reconstruction,” *J. Magn. Reson.*, vol. 318, p. 106790, 2020.
- [5] X. Qu *et al.*, “Accelerated nuclear magnetic resonance spectroscopy with deep learning,” *Angew. Chem. Int. Edit.*, vol. 59, pp. 10297-10300, 2020.
- [6] D. Chen, Z. Wang, D. Guo, V. Orekhov, and X. Qu, “Review and prospect: Deep learning in nuclear magnetic resonance spectroscopy,” *Chem-Eur. J.*, vol. 26, no. 46, pp. 10391-10401, 2020.
- [7] Y. Huang *et al.*, “Exponential signal reconstruction with deep Hankel matrix factorization,” *IEEE Trans. Neural Netw. Learn. Syst.*, DOI: 10.1109/TNNLS.2021.3134717, 2021.
- [8] Z. Wang *et al.*, “A sparse model-inspired deep thresholding network for exponential signal reconstruction-application in fast biological spectroscopy,” *IEEE Trans. Neural Netw. Learn. Syst.*, DOI: 10.1109/TNNLS.2022.3144580, 2022.
- [9] Q. Yang, Z. Wang, K. Guo, C. Cai, and X. Qu, “Physics-driven synthetic data learning for biomedical magnetic resonance: The imaging physics-based data synthesis paradigm for artificial intelligence,” *IEEE Signal Process. Mag.*, DOI: 10.1109/MSP.2022.3183809, 2022.
- [10] E. M. Lawrence, V. J. Gnanapragasam, A. N. Priest, and E. Sala, “The emerging role of diffusion-weighted MRI in prostate cancer management,” *Nat. Rev. Urol.*, vol. 9, no. 2, pp. 94-101, 2012.
- [11] L. Tang, and X. J. Zhou, “Diffusion MRI of cancer: From low to high b-values,” *J. Magn. Reson. Imaging*, vol. 49, no. 1, pp. 23-40, 2019.
- [12] D. Le Bihan, “Looking into the functional architecture of the brain with diffusion MRI,” *Nat. Rev. Neurosci.*, vol. 4, no. 6, pp. 469-480, 2003.
- [13] A. W. Anderson, and J. C. Gore, “Analysis and correction of motion artifacts in diffusion weighted imaging,” *Magn. Reson. Med.*, vol. 32, no. 3, pp. 379-87, 1994.
- [14] Y. Huang *et al.*, “Phase-constrained reconstruction of high-resolution multi-shot diffusion weighted image,” *J. Magn. Reson.*, vol. 312, p. 106690, 2020.
- [15] H. K. Aggarwal, M. P. Mani, and M. Jacob, “MoDL-MUSSELS: Model-based deep learning for multi-shot sensitivity-encoded diffusion MRI,” *IEEE Trans. Med. Imaging*, vol. 39, no. 4, pp. 1268-1277, 2019.
- [16] Y. Hu *et al.*, “RUN-UP: Accelerated multi-shot diffusion-weighted MRI reconstruction using an unrolled network with U-Net as priors,” *Magn. Reson. Med.*, vol. 85, pp. 709-720, 2020.
- [17] C. Qian *et al.*, “A paired phase and magnitude reconstruction for advanced diffusion-weighted imaging,” arXiv:2203.14559, 2022.
- [18] M. Mani, M. Jacob, D. Kelley, and V. Magnotta, “Multi-shot sensitivity-encoded diffusion data recovery using structured low-rank matrix completion (MUSSELS),” *Magn. Reson. Med.*, vol. 78, no. 2, pp. 494-507, 2017.
- [19] M. Uecker *et al.*, “ESPIRiT-an eigenvalue approach to autocalibrating parallel MRI: Where SENSE meets GRAPPA,” *Magn. Reson. Med.*, vol. 71, no. 3, pp. 990-1001, 2014.
- [20] J. P. Haldar, “Low-rank modeling of local k-space neighborhoods (LORAKS) for constrained MRI,” *IEEE Trans. Med. Imaging*, vol. 33, no. 3, pp. 668-681, 2013.
- [21] H. K. Aggarwal, M. P. Mani, and M. Jacob, “MoDL: Model-based deep learning architecture for inverse problems,” *IEEE Trans. Med. Imaging*, vol. 38, no. 2, pp. 394-405, 2018.
- [22] H. Guo *et al.*, “POCS-enhanced inherent correction of motion-induced phase errors (POCS-ICE) for high-resolution multi-shot diffusion MRI,” *Magn. Reson. Med.*, vol. 75, no. 1, pp. 169-180, 2016.
- [23] Q. Huynh-Thu, and M. Ghanbari, “Scope of validity of PSNR in image/video quality assessment,” *Electron. Lett.*, vol. 44, no. 13, pp. 800-801, 2008.